ACS NANO

www.acsnano.org

ARTICLE

DNA Tetrahedra Modules as Versatile Optical Sensing Platforms for Multiplexed Analysis of miRNAs, Endonucleases, and Aptamer–Ligand Complexes

Zhixin Zhou, Yang Sung Sohn, Rachel Nechushtai, and Itamar Willner*

Cite This: *ACS Nano* 2020, 14, 9021–9031

Read Online

ACCESS | Metrics & More | Article Recommendations | Supporting Information

ABSTRACT: The sensing modules for analyzing miRNAs or the endonucleases consist of tetrahedra functionalized with three different fluorophore–quencher pairs in spatially quenched configurations and hairpin units acting as recognition elements for the analytes. Three different miRNAs (miRNA-21, miRNA-221, and miRNA-155) or three different endonucleases (Nt.BbvCI, *Eco*RI, and *Hin*dIII) uncage the respective hairpins, leading to the switched-on fluorescence of the respective fluorophores and to the multiplex detection of the respective analytes. In addition, a tetrahedron module for the multiplexed analysis of aptamer ligand complexes (ligands = ATP, thrombin, VEGF) is introduced. The module includes edges modified with three spatially separated fluorophore–quencher pairs that were stretched by the respective aptamer strands to yield a switched-on fluorescent state. Formation of the respective aptamer ligands reconfigures the edges into fluorophore-quenched caged-hairpin structures that enable the multiplexed analysis of the aptamer–ligand complexes. The facile permeation of the tetrahedra structures into cells is used for the imaging of MCF-7 and HepG2 cancer cells and their discrimination from normal epithelial MCF-10A breast cells.

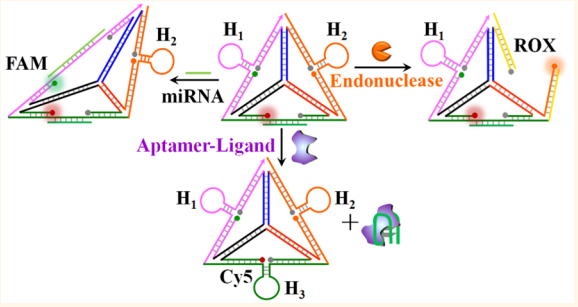

KEYWORDS: *fluorescence, sensors, VEGF, thrombin, DNA nanotechnology*

The development of parallel and multiplexed sensing platforms for the detection of microRNAs, aptamer–ligands, nuclease activities, or DNA has utmost significance for the detection and progress of diseases,[1−3] gene profiling,[4] environmental monitoring,[5,6] detection of pathogens,[7] and biowarfare agents.[8] Different analytical schemes for the multiplexed electrochemical and optical analysis of targets were reported. For example, bar-coded metal microrods generated in alumina channels were suggested for high-throughput analysis.[9] Graphene oxide[10] or transition metal dichalcogenide nanosheets[11] were applied for the multiplexed fluorescence analysis of genes or aptamer–ligands. Also, the size-controlled luminescence properties of semiconductor quantum dots[12,13] or metal nanoclusters, such as Ag nanoclusters,[14,15] were used to develop multiplexed detection schemes. Hybrid conjugates consisting of hemin/G-quadruplex and different-sized semiconductor quantum dots were applied for the multiplexed analysis of genes[16] and aptamer–ligand complexes[17] using chemiluminescence resonance energy transfer (CRET) as the readout signal. Multiplexed electrochemical detection of analytes was achieved by the application of metal nanoparticles[18] or semiconductor nanoparticles[13,19,20] as labeling codes for the sensing events. Also, microfluidic electrochemical aptamer-based assays were integrated on chips for the amplified and multiplexed analysis of aptamer–ligand complexes.[21] In addition, DNA machineries such as the hybridization chain reaction[22] or rolling circle amplification process,[23,24] or the use of multigene DNA scaffolds and polymerization/nicking enzyme machineries, for the autonomous synthesis of DNAzyme-generating specific fluorescent readout signals were used for multiplexed sensing.[25]

The rapidly developing area of DNA nanotechnology[26,27] introduced different nucleic-acid-functionalized nano- and microhybrid carriers, such as nanoparticles,[28−31] metal–

Received: May 14, 2020
Accepted: June 15, 2020
Published: June 15, 2020

https://dx.doi.org/10.1021/acsnano.0c04031
ACS Nano 2020, 14, 9021–9031

Scheme 1. Schematic Multiplexed Analysis of Three Different miRNAs by a Functional DNA Tetrahedra Module

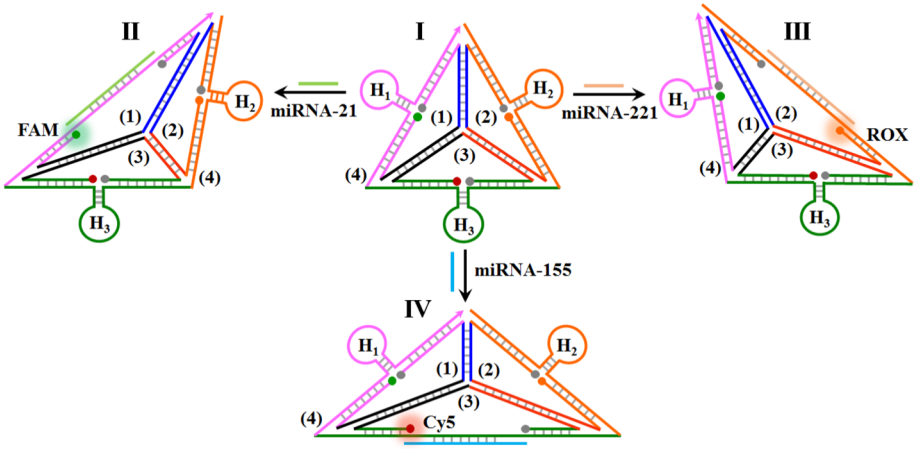

organic framework particles,[32−35] and microcapsules,[36,37] acting as sense-and-treat systems. Also, the dictated hybridization of complementary nucleic acids led to the assembly of supramolecular nanostructures such as origami systems[38,39] or oligomerized crossover junction units.[40,41] The DNA tetrahedron represents a unique three-dimensional nanostructure.[42−44] The possibility to modify the corners of the tetrahedron with different chemical functions, such as different fluorophores, and the feasibility to functionalize the edges of the tetrahedron with nucleic acid functionalities, such as stimuli-responsive or DNAzyme units, allow the programmed reconfiguration of the tetrahedron edges.[45] Indeed, these unique properties of DNA tetrahedra nanostructures were used for the development of electrochemical DNA sensors.[46] In addition, DNA tetrahedra nanostructures revealed effective permeation into living cells,[47,48] and these properties were applied to sense intracellular ingredients,[49] to image cells,[50] and to use the tetrahedron scaffold as a functional unit to amplify miRNA detection in cells.[51]

In the present study, we introduce the DNA tetrahedron module as a versatile unit for diverse parallel and multiplexed sensing applications. We describe the engineering of the edges of the tetrahedra with three different fluorophore−quencher pairs and with predesigned hairpin structures and present the use of the tetrahedra as functional modules for the parallel and multiplexed sensing of different analytes. Specifically, we apply the modules for the multiplexed sensing of miRNAs, of enzymes cleaving DNA (endonucleases), and of ligand−aptamer complexes. In addition, the facile permeation of the tetrahedra structures into cells is used for the imaging of MCF-7 and HepG2 cancer cells and their distinction from normal epithelial MCF-10A breast cells by the fluorophore/quencher-functionalized sensing module.

RESULTS AND DISCUSSION

MicroRNAs (miRNAs) are short noncoding RNA molecules (21−24 bases) that post-transcriptionally regulate gene expression in various cellular processes.[52,53] Particularly misregulated expression of miRNAs is closely correlated with cancer development and progression, thus highlighting the importance of detection of miRNAs for clinical diagnostics.[54−56] Scheme 1 outlines the assembly of the DNA tetrahedron structure for the multiplexed analysis of three different miRNAs. Three nucleic acid strands, **1**, **2**, and **3**, presented schematically as three quasi-triangle structures, are interhybridized by appropriate base-paired domains, and the resulting supramolecular **1**/**2**/**3** structure is further rigidified by a peripheral strand **4** that hybridizes with the single-strand domains of the quasi-triangle edges of **1**, **2**, and **3**. The interhybridized composite **1**/**2**/**3**/**4** forms the resulting tetrahedron nanostructure, state I. The single-strand quasi-triangle edges of **1**, **2** and **3** are modified at their 3′- and 5′-ends with fluorophore/quencher pairs (for **1**, FAM/BHQ1; for **2**, ROX/BHQ2; for **3**, Cy5/BHQ2). The peripheral rigidifying strand, stabilizing the quasi-triangle-shaped units, includes three hairpin components, H_1, H_2, and H_3, where the stem regions of the hairpins are engineered at spatial positions in proximity to the fluorophore/quencher units associated with the quasi-triangles **1**, **2**, and **3**, respectively. Under these conditions, the fluorophores associated with edges of the DNA tetrahedron are quenched. The hairpins H_1, H_2, and H_3 include, in the loop regions, the recognition sequences for miRNA-21, miRNA-221, and miRNA-155, respectively. The method to use the hairpin-functionalized tetrahedron as a functional scaffold for sensing the three different miRNAs, and particularly for the multiplexed analysis of the miRNAs, is also addressed in Scheme 1. Treatment of the rigidified tetrahedron scaffold, state I, with miRNA-21 results in the opening of hairpin H_1 and the distortion of the scaffold, thus forming state II. The formation of the duplex between H_1 and miRNA-21 distorts the shape of the H_1-containing edge, resulting in the spatial separation of the fluorophore/quencher pair (FAM/BHQ1) and the enhanced fluorescence of the FAM (λ = 516 nm). Note that miRNA-21 does not interact with hairpins H_2 and H_3, and thus, the fluorescence of the fluorophores in proximity to hairpins H_2 and H_3 is not affected. Treatment of the sensing platform with miRNA-221 opens hairpin H_2 and generates state III, where the fluorophore/quencher pair (ROX/BHQ2) is separated, and the fluorescence of ROX, λ = 600 nm, is intensified. Also, subjecting the sensing platform to miRNA-155 leads to the opening of hairpin H_3 and to the formation of state IV, where the tetrahedron edge consisting of the fluorophore/quencher pair (Cy5/BHQ2) is stretched. This results in the intensified fluorescence of Cy5, λ = 663 nm. Note that the sensing scaffold, state I, provides a functional nanostructure for the multiplexed analysis of the miRNAs. In the presence of any combination of two miRNAs, or in the presence of all three miRNAs, the respective hairpins are anticipated to be unlocked, leading to the intensified

https://dx.doi.org/10.1021/acsnano.0c04031
ACS Nano 2020, 14, 9021−9031

fluorescence of the fluorophores associated with the respective hairpin-modified edges.

In the first step, the formation of the intact tetrahedron scaffold, state I, and the association of miRNA-155, miRNA-21, and miRNA-221 were confirmed by electrophoretic separation (Figure 1). In lane 1, the band of the quasi-triangle

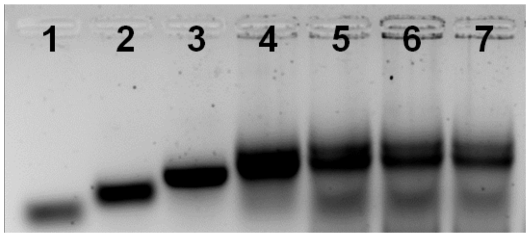

Figure 1. Agarose gel electrophoresis (2%) analysis of the construction of the tetrahedron sensing modules described in Scheme 1. Lane 1, strand 1; lane 2, duplex strand 1 + 2; lane 3, Y-shaped structure consisting of strands 1 + 2 + 3; lane 4, intergrated tetrahedra module composed of 1 + 2 + 3 + 4; lane 5, intergrated tetrahedra modified with miRNA-21; lane 6, intergrated tetrahedra carrying miRNA-155; lane 7, intergrated tetrahedra carrying miRNA-221.

strand **1** is presented. Lanes 2, 3, and 4 show the stepwise construction of the interhybridized structures **1**/**2**, **1**/**2**/**3**, and **1**/**2**/**3**/**4**. The stepwise increase in the molecular weight of the structures leads to slower migration rates. Lanes 5, 6, and 7 depict the bands corresponding to the resulting miRNAs hybridized with the tetrahedron sensing scaffold. It should be noted that the gel electrophoresis shown in Figure 1 demonstrates the intact structure of the tetrahedra modified with each of the miRNA. The electrophoretic studies were further complemented with agarose gel electrophoretic separation, examining the multiplexed detection of the miRNAs (Figure S1 and accompanying discussion).

Figure 2 shows the selective optical (fluorescence) sensing of the three miRNAs by the sensing scaffold, state I. Figure 2A, panel I, shows the fluorescence intensities of FAM before the addition of miRNA-21, curve (a), and after the addition of miRNA-21, 0.2 μM, curve (b). For comparison, curves (c) and (d) show the fluorescence intensities of the sensing platform upon addition of the miRNA-155 and miRNA-221. The fluorescence of FAM is not affected by miRNA-155 and miRNA-221, and the selective intensified fluorescence of FAM is observed upon the miRNA-21-driven unlocking of hairpin H_1. Figure 2A, panel II, shows the fluorescence spectra of FAM upon the treatment of the sensing platform, with different concentrations of miRNA-21. As the concentration of miRNA-21 increases, the fluorescence intensity increases consistently with the enhanced opening of hairpin H_1 associated with the sensing scaffold. Figure 2A, panel III, depicts the calibration curve corresponding to the fluorescence intensities of FAM in the presence of variable concentrations of miRNA-21. The

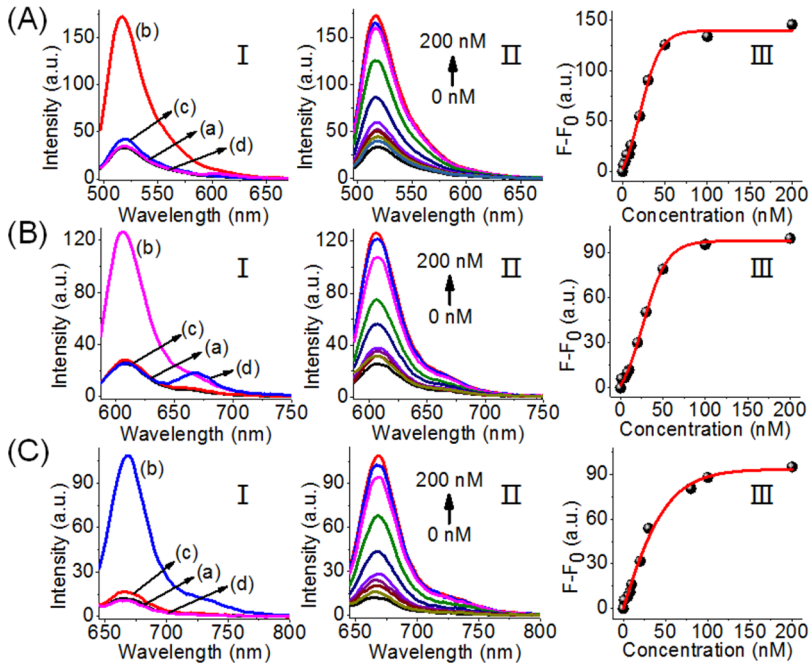

Figure 2. Analysis of three miRNAs by the DNA tetrahedron module described in Scheme 1. (A) Analysis of miRNA-21. Panel I: fluorescence spectra of FAM (a) in the absence of added miRNA-21, (b) upon the addition of miRNA-21, 0.2 μM, (c) upon addition of miRNA-221, 0.2 μM, (d) upon addition of miRNA-155, 0.2 μM. Panel II: fluorescence changes of FAM upon the addition of variable concentrations of miRNA-21. Panel III: derived calibration curve corresponding to the fluorescence changes of FAM at different concentrations of miRNA-21. (B) Analysis of miRNA-221. Panel I: fluorescence spectra of ROX (a) in the absence of added miRNA-221, (b) upon the addition of miRNA-221, 0.2 μM, (c) upon addition of miRNA-21, 0.2 μM, (d) upon addition of miRNA-155, 0.2 μM. Panel II: fluorescence changes of ROX upon the addition of variable concentrations of miRNA-221. Panel III: derived calibration curve corresponding to the fluorescence changes of ROX at different concentrations of miRNA-221. (C) Analysis of miRNA-155. Panel I: fluorescence spectra of Cy5 (a) in the absence of added miRNA-155, (b) upon the addition of miRNA-155, 0.2 μM, (c) upon addition of miRNA-21, 0.2 μM, (d) upon addition of miRNA-221, 0.2 μM. Panel II: fluorescence changes of Cy5 upon the addition of variable concentrations of miRNA-155. Panel III: derived calibration curve corresponding to the fluorescence changes of Cy5 at different concentrations of miRNA-155.

https://dx.doi.org/10.1021/acsnano.0c04031
ACS Nano 2020, 14, 9021−9031

fluorescence intensity of FAM associated with the scaffold levels off at a miRNA-21 concentration corresponding to ~50 nM. The detection limit for sensing miRNA-21 corresponds to 1 nM. Similarly, Figure 2B, panel I, shows the fluorescence spectra of ROX associated with the sensing scaffold in the absence of miRNA-221, curve (a), and in the presence of miRNA-221, 0.2 μM, curve (b). Subjecting the sensing platform to miRNA-221 results in the opening of H_2 and the formation of the asymmetric tetrahedron, state III, where the fluorophore ROX is spatially separated from the quencher unit. The spatial separation of the fluorophore from the quencher leads to the enhanced fluorescence of ROX. Figure 2B, panel I, shows the fluorescence of the fluorophore ROX upon addition of miRNA-21, curve (c), and miRNA-155, curve (d). Only the background fluorescence of the sensing scaffold is observed, implying that the foreign miRNA-21 and miRNA-155 do not interfere or perturb the sensing of miRNA-221. Figure 2C, panel I, depicts the fluorescence spectra of Cy5 associated with the tetrahedron sensing platform in the absence of miRNA-155, curve (a), and in the presence of miRNA-155, 0.2 μM, curve (b). The resulting fluorescence of Cy5 generated by the scaffold upon addition of miRNA-155 is consistent with the opening of hairpin H_3 and the spatial separation of the fluorophore/quencher pair, state IV. As before, subjecting the tetrahedron sensing platform to the foreign miRNA-21 and miRNA-221 does not affect the florescence of Cy5, and only the background fluorescence of Cy5 is observed, curves (c) and (d), respectively. The fluorescence spectra of Cy5 of the sensing platform, in the presence of variable concentrations of miRNA-155, are shown in Figure 2C, panel II, and the calibration curve corresponding to the fluorescence intensity of Cy5, in the presence of variable concentrations of miRNA-155, is presented in Figure 2C, panel III. As the concentrations of miRNA-155 increase, the fluorescence of Cy5 is intensified, and it levels off to a saturation level at a miRNA-155 concentration of ~100 nM. The detection limit for sensing miRNA-155 corresponds to 1 nM. The results indicate that the tetrahedron sensing module, state I, allows the parallel selective detection of the three miRNAs.

The selective fluorescence of the three fluorophores associated with the tetrahedron scaffold suggests that the sensing module could be applied for the multiplexed analysis of the three miRNAs. Figure 3 demonstrates the multiplexed analysis of the set of miRNAs. The fluorescence changes observed upon subjecting the sensing module to miRNA-21 and miRNA-155 are presented in panel I. The fluorescence intensities of FAM (reporter for miRNA-21) and Cy5 (reporter for miRNA-155) are intensified, whereas no fluorescence change of ROX (reporter for miRNA-221) is observed. Multiplexed analysis of miRNA-155 and miRNA-221 is reflected by high fluorescence changes of Cy5 and ROX and lack of any fluorescence changes of FAM. In addition, panel III demonstrates the multiplexed analysis of miRNA-221 and miRNA-21. Finally, panel IV depicts the multiplexed analysis of all three miRNAs. In this experiment, the sensing module is subjected to miRNA-155, miRNA-21, and miRNA-221. The fluorescence intensities of FAM, ROX, and Cy5 are intensified, demonstrating that the parallel multiplexed detection of all three miRNAs is, indeed, feasible.

Although the DNA tetrahedra structure provides an elegant nanostructure for the multiplexed analysis of miRNAs, one could argue that the same analytical challenge may be demonstrated by other mixtures of sensing probes, such as a

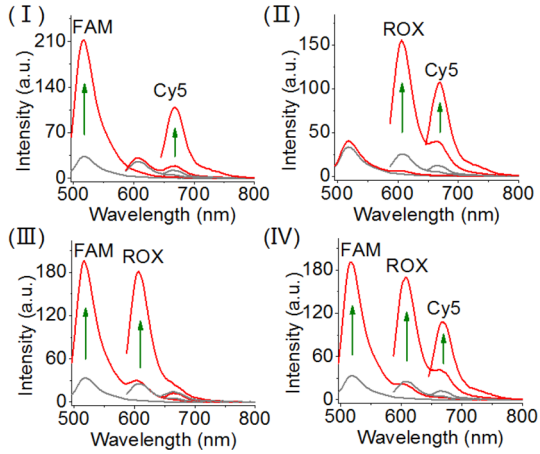

Figure 3. Multiplexed analysis of the three miRNA targets, miRNA-21, miRNA-221, and miRNA-155 by the DNA tetrahedron sensing module. Panel I: sensing of miRNA-21 and miRNA-155, switches on the fluorescence of FAM and Cy5. Panel II: sensing miRNA-221 and miRNA-155 by the sensing module, switches on the fluorescence of ROX and Cy5. Panel III: sensing miRNA-21 and miRNA-221 by the sensing module, switches on the fluorescence of FAM and ROX. Panel IV: multiplexed sensing of all three miRNAs (miRNA-21, miRNA-221, and miRNA-155), switches on the fluorescence of FAM, ROX, and Cy5. The concentrations of each of the miRNAs in the systems correspond to 0.2 μM.

mixture of three different hairpins modified with three different fluorophore/quencher pairs. We feel, however, that the applications of an integrated functional tetrahedron nanostructure for the multiplexed parallel analysis of three miRNAs could reveal significant biosensing and imaging advantages due to the easy, high-yield, permeation of the DNA tetrahedra into cells. This is demonstrated in Figure 4 with the multiplexed analysis of miRNA-21 and miRNA-155 in two types of cancer cells (*e.g.*, MCF-7 breast cancer cells, HepG2 liver cancer cells), in comparison to normal epithelial breast cells MCF-10A. The MCF-7 cells include the miRNA-21 and miRNA-155 as biomarkers,[57] and the HepG2 cells overexpress miRNA-

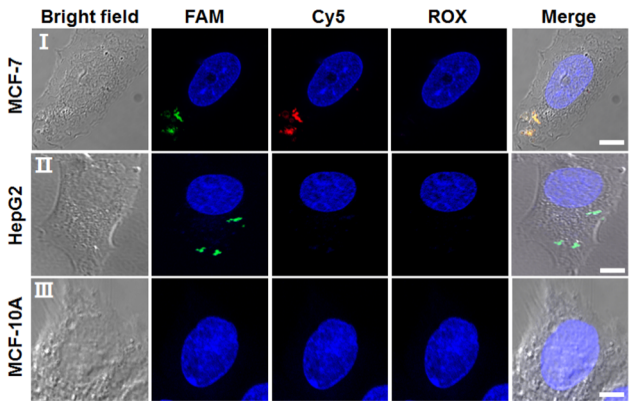

Figure 4. Bright-field microscopy images, confocal fluorescence microscopy images, and merge images corresponding to the analysis of (entry I) MCF-7 cells, (entry II) HepG2 cells, (entry III) MCF-10A cells treated with the FAM/Cy5/ROX-functionalized tetrahedra. The fluorescence of the three fluorescent probes is imaged through three channels: FAM emission, λ_{ex} = 488 nm; Cy5 emission, λ_{ex} = 640 nm; ROX emission, λ_{ex} = 561 nm. Scale bar: 5 μm.

https://dx.doi.org/10.1021/acsnano.0c04031
ACS Nano 2020, 14, 9021−9031

Scheme 2. Schematic Multiplexed Analysis of Three Different Endonucleases Operating on a DNA Tetrahedra Module

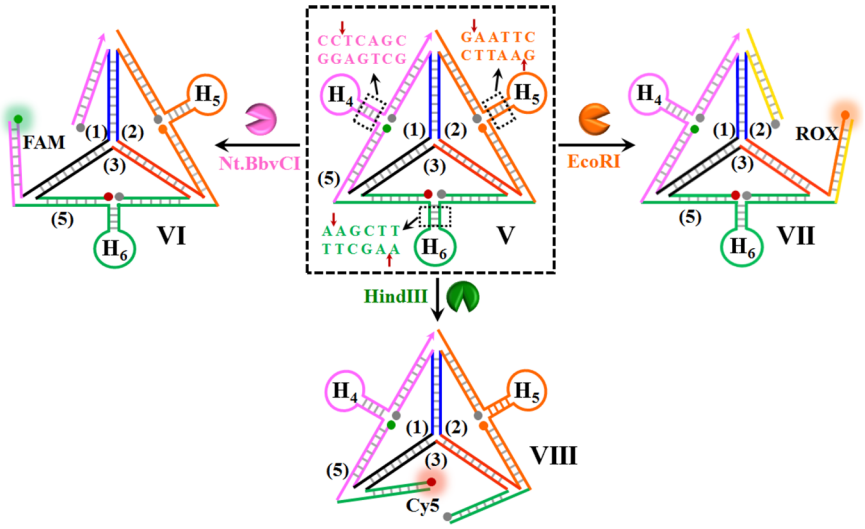

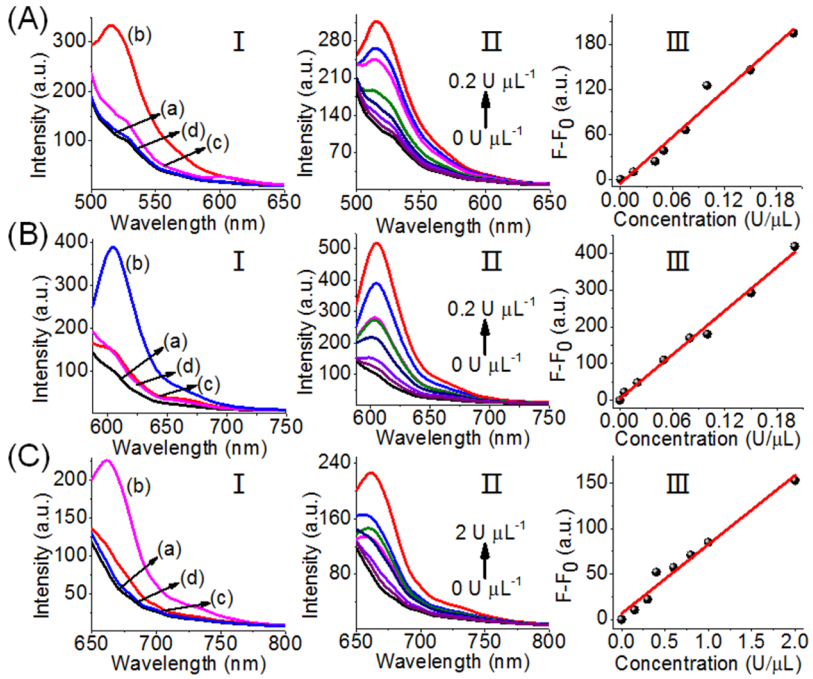

Figure 5. Analysis of three endonucleases by the DNA tetrahedron module shown in Scheme 2. (A) Analysis of Nt.BbvCI. Panel I: fluorescence spectra of FAM (a) in the absence of added Nt.BbvCI, (b) upon the addition of Nt.BbvCI, 0.2 U μL^{-1}, (c) upon addition of *Eco*RI, 0.2 U μL^{-1}, (d) upon addition of *Hin*dIII, 0.2 U μL^{-1}. Panel II: fluorescence changes of FAM upon the addition of variable concentrations of Nt.BbvCI. Panel III: derived calibration curve corresponding to the fluorescence changes of FAM at different concentrations of Nt.BbvCI. (B) Analysis of *Eco*RI. Panel I: fluorescence spectra of ROX (a) in the absence of added *Eco*RI, (b) upon the addition of *Eco*RI, 0.16 U μL^{-1}, (c) upon addition of Nt.BbvCI, 0.16 U μL^{-1}, (d) upon addition of *Hin*dIII, 0.16 U μL^{-1}. Panel II: fluorescence changes of ROX upon the addition of variable concentrations of *Eco*RI. Panel III: derived calibration curve corresponding to the fluorescence changes of ROX at different concentrations of *Eco*RI. (C) Analysis of *Hin*dIII. Panel I: fluorescence spectra of Cy5 (a) in the absence of added *Hin*dIII, (b) upon the addition of *Hin*dIII, 2 U μL^{-1}, (c) upon addition of Nt.BbvCI, 2 U μL^{-1}, (d) upon addition of *Eco*RI, 2 U μL^{-1}. Panel II: fluorescence changes of Cy5 upon the addition of variable concentrations of *Hin*dIII. Panel III: derived calibration curve corresponding to the fluorescence changes of Cy5 at different concentrations of *Hin*dIII.

21.[58] Accordingly, the different cells were treated with the tetrahedra composite shown in Scheme 1 that includes three quenched fluorophores, FAM, Cy5, and ROX. Figure 4, entry I, shows the bright-field image and confocal fluorescence microscopy images of the MCF-7 cell recorded at the excitation wavelengths of the different fluorophores associated with the tetrahedra. The green FAM fluorescence corresponding to miRNA-21 and red Cy5 fluorescence corresponding to miRNA-155 are observed, and the ROX fluorescence corresponding to miRNA-221 cannot be detected. The merged image (yellow) confirms the generation of the green and red fluorescence by the tetrahedra. Figure 4, entry II, shows the bright-field microscopy image, the confocal fluorescence microscopy images at the three emission wavelengths, and the merge image of the HepG2 cells treated with the tetrahedra. Only the green fluorescence of FAM can be

https://dx.doi.org/10.1021/acsnano.0c04031
ACS Nano 2020, 14, 9021−9031

detected, and no Cy5 or ROX emission can be observed (merged green image). These results are consistent with the overexpression of miRNA-21 in the HepG2 cells. Figure 4, entry III, shows the bright-field microscopy image, the confocal fluorescence microscopy images at the three fluorophore imaging wavelengths, and the merge image of the MCF-10A cells treated with the tetrahedra. No fluorescence of the fluorophore probes associated with the tetrahedra is observed, consistent with the low expression of miRNA-21 or miRNA-155 in the MCF-10A cells (for large-area confocal fluorescence microscopy image of the different cells, see Figure S2, Supporting Information).

The tetrahedron sensing module appears to be a versatile sensing scaffold. By the appropriate engineering of the hairpin units associated with the module, other targets can be analyzed and detected in parallel. Scheme 2 presents the application of the tetrahedron scaffold to analyze enzymes that catalyze the cleavage of DNA. DNA cleavage by endonucleases is not only essential during cellular events and physiological processes, such as DNA replication or repair,[59] but also extensively used as a powerful tool in PCR and molecular cloning.[60] Thus, assaying of endonuclease activities is of significant importance in the fields of molecular biology and clinical diagnosis.[61,62] As a proof of concept, three endonucleases, *Eco*RI, Nt.BbvCI, and *Hin*dIII, are analyzed in the present study. The sensing module includes, as before, the single strands **1**, **2**, and **3** functionalized with the different fluorophore/quencher pairs, and these are presented as three quasi-triangle structures exhibiting interhybridization domains. The three interhybridized quasi-triangles are rigidified by the peripheral strand **5** that includes, at the edges of the resulting tetrahedron, the hairpins H_4, H_5, and H_6. The hairpins H_4, H_5, and H_6 include duplex stem domains that are cleaved by the respective enzymes. In the rigidified tetrahedron structure, state V, all of the fluorophores exist in a quenched configuration. Subjecting the sensing module to Nt.BbvCI results in the cleavage of the stem region associated with hairpin H_4. The cleavage of the hairpin associated with the respective edge results in a flexible edge, state VI, where the fluorophore FAM is spatially separated from the quencher unit. This leads to the switching-on fluorescence of FAM. Similarly, the treatment of the tetrahedron module with *Eco*RI leads to the cleavage of the stem domain of hairpin H_5, and this transforms the H_5-modified edge into a broken domain where the fluorophore ROX is spatially separated from the quencher, state VII. The flexibility of this edge is anticipated to switch on the luminescence of ROX. In addition, subjecting the sensing module to *Hin*dIII results in the base-specific nicking of one strand of the stem region of hairpin H_6. The cleavage of the stem strand separates the hairpin and introduces functional flexibility into the H_6 carrying edge. The separation of the rigidifying strand of this edge leads to a flexible structure of the domain, resulting in the spatial separation of the fluorophore Cy5 from the quencher unit, state VIII. As a result, the fluorescence of Cy5 is switched on.

Figure 5A, panel I, shows the fluorescence spectra of the sensing module before interaction with Nt.BbvCI, curve (a), and after subjecting the sensing scaffold to Nt.BbvCI, 0.2 U μL^{-1}, curve (b). Subjecting the sensing module to Nt.BbvCI leads to the triggered-on fluorescence of FAM, implying that hairpin H_4 carrying edge was, indeed, cleaved, and the resulting flexibility and accompanied spatial separation of the fluorophore and quencher unit lead to the triggered-on fluorescence of FAM. Panel I, curves (c) and (d), show the effect of added *Hin*dIII or *Eco*RI catalyst, each at a concentration of 0.2 U μL^{-1}, on the fluorescence of the fluorophore FAM. The fluorescence intensities of FAM are almost identical to the initial fluorescence intensity of FAM prior to the addition of Nt.BbvCI. Thus, although the addition of *Hin*dIII or *Eco*RI leads to structural transformation at other edges of the tetrahedron (*vide infra*), the fluorescence of FAM stays quenched in the presence of the other two biocatalysts. This indicates that the rigidified structure FAM/quencher is preserved, even though structural perturbations take place on remote edges associated with the tetrahedron structure. That is, the inner Y-shaped hybridization between the quasi-triangle subunits **1**, **2**, and **3** retains the basic skeleton, even though rigidified edges of the tetrahedron are broken. Figure 5A, panels II and III, show fluorescence changes of the sensing module upon its challenging with variable concentrations of Nt.BbvCI and the derived calibration curve, respectively. As the concentration of Nt.BbvCI increases, the fluorescence of FAM is intensified, consistent with the enhanced cleavage of the H_4 carrying edge. Figure 5B, panel I, shows the fluorescence intensities of the fluorophore ROX, associated with the hairpin H_5 carrying edge before treatment with *Eco*RI, curve (a), and after interaction with *Eco*RI, 0.16 U μL^{-1}, curve (b). The addition of *Eco*RI results in the increased fluorescence of ROX, consistent with the *Eco*RI-stimulated cleavage of the hairpin H_5 carrying edge and the accompanying spatial separation between the fluorophore ROX and quencher unit. Treatment of the sensing scaffold with Nt.BbvCI or *Hin*dIII does not affect the fluorescence of ROX, panel I, curves (c) and (d). Thus, although these biocatalysts induce structural transitions on the H_4- and H_6-hairpin-carrying edges, the quenched fluorescence of ROX is not affected. These results imply that the interhybridized Y-shaped structure of **1**/**2**/**3** stays intact, even though structural perturbations on the H_4- or H_6-haipin-carrying edges proceed. Figure 5B, panels II and III, show the fluorescence of ROX upon treatment of the sensing module with different concentrations of *Eco*RI and the derived calibration curve, respectively. The fluorescence intensities of ROX increase as the concentrations of *Eco*RI are elevated, consistent with the enhanced cleavage of the H_5-carrying edge. The results demonstrate that the fluorescence changes of ROX are selective toward the sensing of *Eco*RI. Figure 5C, panel I, shows the fluorescence changes of the sensing module at fluorescence of Cy5 before its treatment with *Hin*dIII, curve (a), and after interaction of the sensing scaffold with the biocatalyst, 2.0 U μL^{-1}, curve (b). The fluorescence of Cy5 is intensified, consistent with the cleavage of the tetrahedron edge carrying hairpin H_6, state VIII. Subjecting the sensing module to the enzymes *Eco*RI or Nt.BbvCI does not affect the fluorescence of Cy5 curves (c) and (d). Thus, although the biocatalysts *Eco*RI and Nt.BbvCI are active in the cleavage of other domains, the fluorescence of Cy5 is not affected, implying that the fluorophore Cy5 is retained in its quenched configuration. Thus, beyond the selective sensing of *Hin*dIII, the results imply that the interhybridization of the Y-shaped domains of **1**/**2**/**3** retains their supramolecular structures. Figure 5C, panels II and III, show the fluorescence changes of the Cy5 reporter unit upon challenging the sensing module with different concentrations of *Hin*dIII and the resulting calibration curve, respectively. As the concentration of *Hin*dIII increases, the fluorescence of Cy5 is enhanced, consistent with higher degree of cleavage of the H_6-carrying edge of the sensing module.

https://dx.doi.org/10.1021/acsnano.0c04031
ACS Nano 2020, 14, 9021−9031

The selective sensing of each of the enzyme-DNA-cleaving biocatalysts by the three-fluorophore-functionalized tetrahedron sensing module, Scheme 2, suggests that the multiplexed analysis of the enzymes should be feasible. Figure 6 shows the

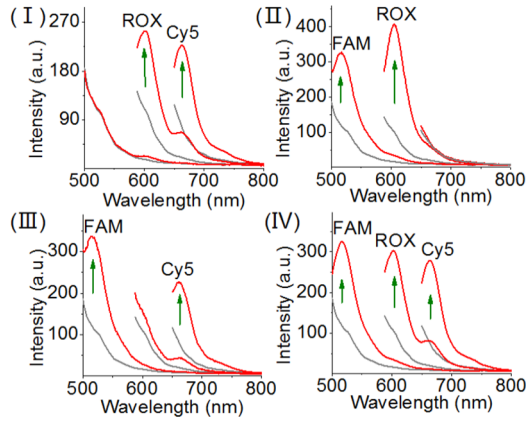

Figure 6. Multiplexed analysis of the three endonuclease, Nt.BbvCI, *Eco*RI, and *Hin*dIII by the DNA tetrahedron module shown in Scheme 2. Panel I: sensing of *Eco*RI and *Hin*dIII, switches on the fluorescence of ROX and Cy5. Panel II: sensing Nt.BbvCI and *Eco*RI by the sensing module, switches on the fluorescence of FAM and ROX. Panel III: sensing Nt.BbvCI and *Hin*dIII by the sensing module, switches on the fluorescence of FAM and Cy5. Panel IV: multiplexed sensing of all three endonucleases: Nt.BbvCI, *Eco*RI, and *Hin*dIII, switches on the fluorescence of FAM, ROX, and Cy5. In all experiments, the concentrations of Nt.BbvCI, *Eco*RI, and *Hin*dIII corresponded to 0.2, 0.2, and 2 U μL^{-1}, respectively.

multiplexed analysis of the three enzymes by the tetrahedron module. Treatment of the sensing module with the two enzymes *Eco*RI and *Hin*dIII results in the fluorescence signals of the H_5- and H_6-hairpin-carrying edges corresponding to ROX and to Cy5. No fluorescence of FAM is detected, indicating that the H_4 hairpin edge reporter is in the caged (quenched) state. Figure 6, panel II, depicts multiplexed analysis of *Eco*RI and Nt.BbvCI by the tetrahedra sensing platform. Treatment of the sensing module with the two enzymes yields the fluorescence of FAM and ROX, yet no fluorescence of Cy5 is observed, implying the H_6-hairpin-caged fluorophore is retained upon sensing of the two enzymes. Also, Figure 6, panel III, shows the fluorescence bands of FAM and Cy5 upon sensing *Hin*dIII and Nt.BbvCI. No fluorescence of ROX is observed, indicating that the *Eco*RI-responsive H_5-caged is retained under these conditions (fluorescence of ROX is quenched). Finally, panel IV depicts the fluorescence features of the tetrahedron sensing module in the presence of all three enzymes. All three fluorescence bands of FAM, ROX, and Cy5 are observed, demonstrating the successful multiplexed analysis of the three enzymes.

The generality of the tetrahedron module for the development of multiplexed sensing platforms was further demonstrated by the application of the tetrahedron scaffold for the multiplexed analysis of aptamer–ligands. Aptamers are sequence-specific nucleic acids generated by the SELEX (systematic evolution of ligands by exponential enrichment) process, which recognize low molecular weight substrates, proteins, and even cells.[63,64] Different optical,[65,66] electrochemical,[67−69] and microgravimetric aptamer–ligand[70] sensing platforms (aptasensors) were developed, and their bioanalytical and biomedical applications, particularly, multiplexed aptasensor configurations, were discussed.[71,72] Scheme 3

Scheme 3. Schematic Multiplexed Analysis of Three Aptamer–Ligands: Ligands = ATP, VEG,F and Thrombin by Tetrahedron Module (Note the Sensing Processes Are Accompanied by a Fluorescence Decrease, in Contrast to Previous Systems)

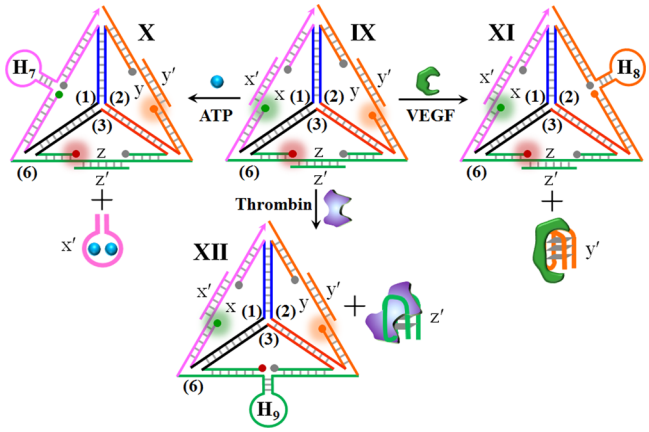

shows the development of tetrahedron sensing module for the parallel detection of an aptamer–ligand. The tetrahedron core consists of the triangle strands **1**/**2**/**3** and the long-strand **6** rigidifying the tetrahedron structure, state IX. The peripheral rigidifying strand **6** includes single-strand domains *x*, *y*, and *z*, and these are further hybridized with auxiliary strands *x*′, *y*′, and *z*′. This hybridization pattern yields a rigidified tetrahedron structure. Nonetheless, in contrast to the previous sensing modules that included fluorophore-quenched edges due to the proximity position of the fluorophore–quencher pairs, dictated by the peripheral rigidifying strand, in the present sensing module, the long and rigid duplex domains *x*/*x*′, *y*/*y*′, and *z*/*z*′ force the fluorophore–quencher pairs into spatially separated positions. Thus, the sensing module exhibits the selectively separated fluorescence bands of FAM, ROX, and Cy5, associated with the respective edges of the rigidified tetrahedron. The strands *x*′, *y*′, and *z*′ correspond to anti-ATP–aptamer, anti-VEGF–aptamer, and antithrombin aptamer, respectively. The parallel sensing principle of the different ligands is also detailed in the Scheme 3. In the presence of the ATP, the strand *x*′ is displaced in the form of the aptamer–ATP complex. The resulting single-strand *x* is pre-engineered to reconfigure after the displacement of *x*′ into the hairpin structure H_7. The rigidification of the hairpin structure leads then to the forced proximity between the fluorophore and quencher on the H_7-carrying edge, resulting in the fluorescence quenching of FAM, state X. Similarly, subjecting the sensing module to VEGF leads to the displacement of *y*′, through the formation of the aptamer–VEGF complex, state XI. This results in the reconfiguration of the single-strand domain into the hairpin H_8. This leads to the close proximity between fluorophore (ROX) and the quencher, resulting in the quenching of the fluorophore. In addition, subjecting the sensing module to thrombin leads to the displacement of strand *z*′ through the formation of the aptamer–thrombin complex, state XII. The reconfiguration into the hairpin structure, H_9, where the fluorophore (Cy5) and quencher are forced into close proximity that leads to

https://dx.doi.org/10.1021/acsnano.0c04031
ACS Nano 2020, 14, 9021−9031

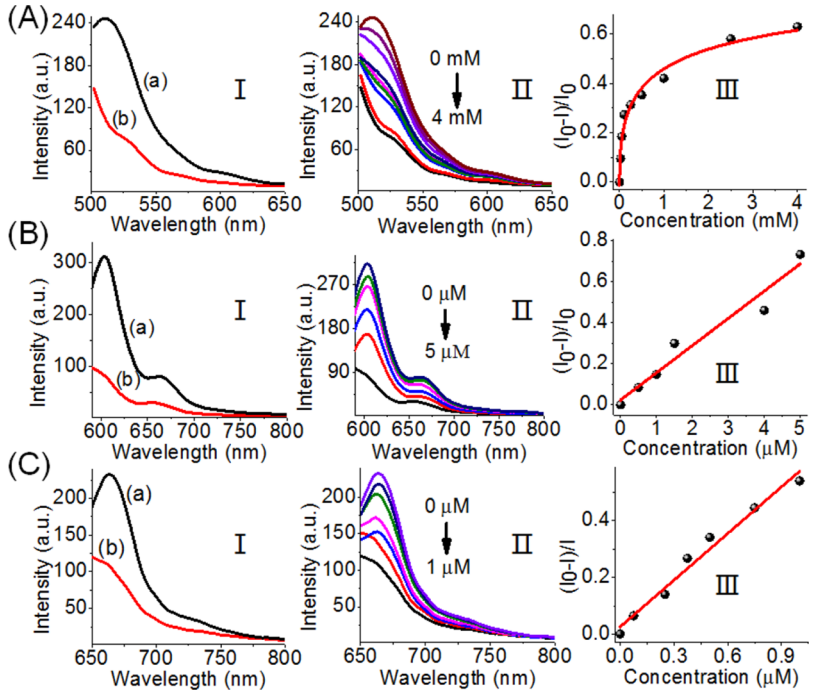

Figure 7. Analysis of three aptamer–ligands by the DNA tetrahedron module shown in Scheme 3. (A) Sensing of ATP by the DNA tetrahedron module. Panel I: fluorescence spectra of FAM before addition of ATP (a) and after the addition of ATP, 4 mM (b). Panel II: fluorescence changes of FAM upon interaction with different concentrations of ATP. Panel III: derived calibration curve corresponding to the fluorescence changes of FAM in the presence of variable concentrations of ATP. (B) Sensing of VEGF by the DNA tetrahedron module. Panel I: fluorescence spectra of ROX before addition of VEGF (a) and after the addition of VEGF, 5 μM (b). Panel II: fluorescence changes of ROX upon interaction with different concentrations of VEGF. Panel III: derived calibration curve corresponding to the fluorescence changes of ROX in the presence of variable concentrations of VEGF. (C) Sensing of thrombin by the DNA tetrahedron module. Panel I: fluorescence spectra of Cy5 before addition of thrombin (a) and after the addition of thrombin, 1 μM (b). Panel II: fluorescence changes of Cy5 upon interaction with different concentrations of thrombin. Panel III: derived calibration curve corresponding to the fluorescence changes of Cy5 in the presence of variable concentrations of thrombin.

effective quenching of the fluorophore, state XII. Note that the sensing of the respective ligands involves a negative fluorescence readout.

Figure 7 depicts the parallel analysis of the three ligands by the tetrahedron scaffold. Figure 7A, panel I, shows the fluorescence features of the sensing module at FAM fluorophore emission before addition of ATP, curve (a), and after the addition of ATP, 4 mM, curve (b). The fluorescence of FAM is quenched, consistent with the separation of the ATP–aptamer and the reconfiguration of the H_7-carrying hairpin on the edge of the tetrahedron, state X. Figure 7A, panel II, shows the fluorescence intensities of FAM upon the addition of variable concentrations of ATP. As the concentrations of ATP increase, the quenching degree of the fluorescence of FAM is enhanced, consistent with the higher degree of the reconfigured H_7-carrying edge, state X. It should be noted that the addition of either thrombin or VEGF to the tetrahedron sensing module does not have any effect on the fluorescence of FAM, even though their ligands have an effect on the reconfiguration of other domains of the tetrahedron module (see Figure S3). Figure 7B, panel I, shows the fluorescence of ROX associated with the sensing module before the addition of VEGF, curve (a), and after the addition of VEGF, 5 μM, curve (b). The fluorescence of ROX is quenched, consistent with the reconfiguration of the sensing module in state XI, where the dissociation of the anti-VEGF–aptamer resulted in the reconfiguration into the H_8 tetrahedron carrying the H_8-hairpin-modified edge. The addition of ATP or thrombin to the sensing module has no effect on the fluorescence of ROX, indicating that the fluorescence quenching is specific to the VEGF analyte (see Figure S3). Figure 7B, panel II, shows the gradual fluorescence changes of ROX upon increasing the concentrations of VEGF. As the concentrations of VEGF increase, the fluorescence quenching is enhanced. Figure 7B, panel III, reveals the derived calibration curve for the analysis of VEGF by the tetrahedron sensing module. Figure 7C, panel I, shows the fluorescence changes of Cy5 associated with the sensing module before treatment with thrombin, curve (a), and after treatment with thrombin, 1 μM, curve (b). The interaction of the sensing scaffold with thrombin leads to the quenching of Cy5, consistent with the displacement of the antithrombin aptamer from the module and the reconfiguration of the domain *z* into the hairpin H_9, where the fluorophore Cy5 and the quencher units are forced into close proximity, state XII. The fluorescence of Cy5 is not affected by the addition of ATP or VEGF to the sensing scaffold, indicating that the observed changes in the fluorescence of Cy5 are specific to the formation of the thrombin–aptamer complex (see Figure S3). Figure 7C, panels II and III, show the fluorescence changes upon treatment of the sensing module with variable concentrations of thrombin and the derived calibration curve, respectively. The changes in the fluorescence intensities increase as the concentrations of thrombin are elevated.

The specific fluorescence changes transduced by the tetrahedron module in response to the respective ligands

https://dx.doi.org/10.1021/acsnano.0c04031
ACS Nano 2020, 14, 9021–9031

(thrombin, ATP, VEGF) were then applied to demonstrate the multiplexed analysis of the ligands (Figure 8). Treatment of

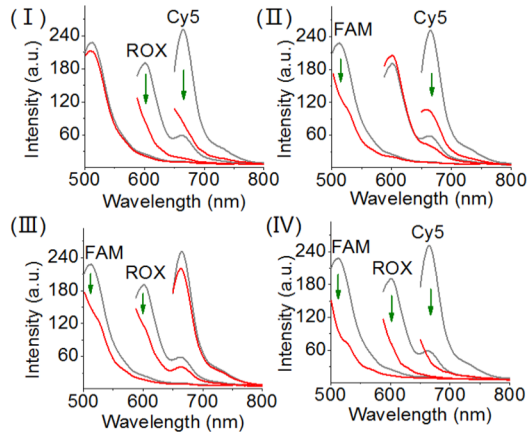

Figure 8. Multiplexed analysis of the three aptamer–ligands, ATP, VEGF, and thrombin by the DNA tetrahedron module shown in Scheme 3. Panel I: sensing of VEGF and thrombin, switches off the fluorescence of ROX and Cy5. Panel II: sensing ATP and thrombin by the sensing module, switches off the fluorescence of FAM and Cy5. Panel III: sensing ATP and VEGF by the sensing module, switches off the fluorescence of FAM and ROX. Panel IV: multiplexed sensing of all three aptamer–ligands: ATP, VEGF, and thrombin, switches off the fluorescence of FAM, ROX, and Cy5.

the sensing scaffold with VEGF and thrombin results in the complete quenching of the fluorophore ROX and Cy5, whereas only a minute change in the fluorescence of FAM is observed (Figure 8, panel I). The results are consistent with the VEGF- and thrombin-driven displacement of the strand y' and z' in the form of the respective ligand–aptamer complexes and the reconfiguration of the hairpins H_8 and H_9 on the respective edges, leading to the effective quenching of ROX and Cy5. Under these conditions, the tetrahedron edge containing the x/x' duplex is unaffected, resulting in the FAM fluorescence intensity characteristic to the parent tetrahedron. Similarly, subjecting the sensing module to the ligands ATP and thrombin leads to the quenching of the fluorescence of FAM and Cy5, whereas the fluorescence of ROX is unaffected. These results are consistent with the displacement of the strand x' (by ATP) and of strand z' (by thrombin) and the reconfiguration of the tetrahedron into the H_7- and H_9-hairpin-carrying edges. Also, Figure 8, panel III, shows the quenching fluorescence of FAM and ROX upon sensing ATP and VEGF. No fluorescence change of Cy5 is observed, indicating that the tetrahedron edge containing the z/z' duplex is unaffected. Finally, the sensing module interacted with all ligand–analytes here (Figure 8, panel IV). All three fluorophore labels are quenched, demonstrating the multiplexed analysis of the three aptamer–ligand complexes.

CONCLUSION

The study has introduced a versatile sensing module consisting of a DNA tetrahedron for the parallel and multiplexed analysis of different targets. In the present study, we engineered sensing modules for miRNAs, DNA-cleaving enzymes, and aptamer–ligands. These concepts can be, however, extended to other analytes, such as genes or metal ions. In the present study, we applied three fluorophores as the transducers of the parallel and multiplex analysis of the different analytes. By designing tetrahedra structures modified with other fluorophores and generating mixture of tetrahedra, the design of parallel and multiplexed sensing platforms of enhanced complexities may by envisaged. The facile permeation of the tetrahedra structure into cells was successfully applied to image MCF-7 and HepG2 cancer cells and their discrimination from the normal epithielial breast cell, MCF-10A, by a single sensing module.

EXPERIMENTAL SECTION

Preparation of the DNA Tetrahedron Module. For miRNA detection, four oligonucleotide strands including **1**, **2**, **3**, and **4**, 1 μM each was mixed in Tris-borate-EDTA (0.5× TBE) buffer containing 50 mM $MgCl_2$, heated to 95 °C for 3 min, and then immediately cooled to 4 °C within 1 min. For enzyme detection, four oligonucleotide strands including **1**, **2**, **3**, and **5**, 1 μM each was mixed in 1× NEBuffer 2 (10 mM Tris, 20 mM $MgCl_2$, 50 mM NaCl, 1 mM DTT and pH 7.9), heated to 95 °C for 3 min, and then immediately cooled to 4 °C within 1 min. For aptamer–ligand detection, seven oligonucleotide strands including 1 μM of **1**, **2**, **3**, **6** and 1.5 μM of x' y', and z' were mixed in 1× NEBuffer 2 (10 mM Tris, 20 mM $MgCl_2$, 50 mM NaCl, 1 mM DTT and pH 7.9), heated to 95 °C for 3 min, and then immediately cooled to 4 °C within 1 min.

Fluorescence Analysis. For detection of miRNAs, different concentrations of miRNAs were added to 100 μL of Tris-borate-EDTA (0.5× TBE) buffer solution (50 mM $MgCl_2$) containing 100 nM DNA tetrahedron module, followed by incubation for 5 min at room temperature. For detection of enzymes, different concentrations of enzymes were added to 200 μL of 1× NEBuffer 2 (10 mM Tris, 10 mM $MgCl_2$, 50 mM NaCl, 1 mM DTT and pH 7.9), containing 90 nM DNA tetrahedron module, followed by incubation for 12 h at room temperature. For detection of aptamer–ligands, different concentrations of aptamer–ligands were added to 200 μL of 1× NEBuffer 2 (10 mM Tris, 10 mM $MgCl_2$, 50 mM NaCl, 1 mM DTT and pH 7.9), containing 90 nM DNA tetrahedron module, followed by incubation for 30 min at room temperature.

Cell Culture. Human breast cancer cells (MCF-7) were grown in 5% CO_2 RPMI-1640 medium supplemented with 10% FCS, L-glutamine, and antibiotics (Biological Industries). Human liver cancer cell line (HepG2) were grown in 5% CO_2 DMEM medium supplemented with 10% FCS, L-glutamine, and antibiotics (Biological Industries). Normal breast cells (MCF-10A) were maintained in complete growth medium consisting of 1:1 mixture of Dulbecco's modified Eagle's medium and Ham's F12 medium supplemented with horse serum (5%), epidermal growth factor (20 ng/mL), cholera toxin (CT, 0.1 μg/mg), insulin (10 μg/mL), hydrocortisone (500 ng/mL), and penicillin/streptomycin (1 unit/mL). Cells were plated 1 day prior to the experiment on a μ-slide 4-well glass bottom dish (ibidi) for confocal microscopy.

Confocal Microscopy Measurements. For cell imaging experiments, cells were planted on a μ-slide 4-well glass bottom dish (ibidi). Cells were incubated with the DNA tetrahedron nanostructures after being washed with phosphate-buffered saline. The three samples of DNA tetrahedra (300 nM) were incubated with cells for 5 h and then washed with DMEM/Hepes twice and replenished with the fresh medium for the measurement. The fluorescence of tetrahedra in cells was monitored with an Olympus FV3000 confocal laser scanning microscope, and all images were analyzed with ImageJ.

ASSOCIATED CONTENT

Supporting Information

The Supporting Information is available free of charge at https://pubs.acs.org/doi/10.1021/acsnano.0c04031.

Nucleic acid sequences, materials, measurement methods, agarose gel for multiplex detection of miRNAs, large-area confocal fluorescence images, and additional fluorescence spectra of aptamer–ligand detection (PDF)

https://dx.doi.org/10.1021/acsnano.0c04031
ACS Nano 2020, 14, 9021–9031

AUTHOR INFORMATION

Corresponding Author

Itamar Willner − *Institute of Chemistry, The Minerva Center for Biohybrid Complex Systems, The Hebrew University of Jerusalem, Jerusalem 91904, Israel;* orcid.org/0000-0001-9710-9077; Email: willnea@vms.huji.ac.il

Authors

Zhixin Zhou − *Institute of Chemistry, The Minerva Center for Biohybrid Complex Systems, The Hebrew University of Jerusalem, Jerusalem 91904, Israel;* orcid.org/0000-0003-0450-1921

Yang Sung Sohn − *Institute of Life Sciences, The Hebrew University of Jerusalem, Jerusalem 91904, Israel*

Rachel Nechushtai − *Institute of Life Sciences, The Hebrew University of Jerusalem, Jerusalem 91904, Israel*

Complete contact information is available at: https://pubs.acs.org/10.1021/acsnano.0c04031

Notes

The authors declare no competing financial interest.

ACKNOWLEDGMENTS

This study is supported by the Israel Science Foundation and the Minerva Center for Biohybrid Complex Systems.

REFERENCES

(1) Han, M.; Gao, X.; Su, J. Z.; Nie, S. Quantum-Dot-Tagged Microbeads for Multiplexed Optical Coding of Biomolecules. *Nat. Biotechnol.* **2001**, *19*, 631−635.

(2) Lockhart, D. J.; Winzeler, E. A. Genomics, Gene Expression and DNA Arrays. *Nature* **2000**, *405*, 827−836.

(3) Xiao, M.; Lai, W.; Man, T.; Chang, B.; Li, L.; Chandrasekaran, A. R.; Pei, H. Rationally Engineered Nucleic Acid Architectures for Biosensing Applications. *Chem. Rev.* **2019**, *119*, 11631−11717.

(4) Stoeva, S. I.; Lee, J.-S.; Thaxton, C. S.; Mirkin, C. A. Multiplexed DNA Detection with Biobarcoded Nanoparticle Probes. *Angew. Chem., Int. Ed.* **2006**, *45*, 3303−3306.

(5) Heller, M. J. DNA Microarray Technology: Devices, Systems, and Applications. *Annu. Rev. Biomed. Eng.* **2002**, *4*, 129−153.

(6) Liu, J.; Cao, Z.; Lu, Y. Functional Nucleic Acid Sensors. *Chem. Rev.* **2009**, *109*, 1948−1998.

(7) Giri, S.; Sykes, E. A.; Jennings, T. L.; Chan, W. C. W. Rapid Screening of Genetic Biomarkers of Infectious Agents Using Quantum Dot Barcodes. *ACS Nano* **2011**, *5*, 1580−1587.

(8) Song, L.; Ahn, S.; Walt, D. R. Fiber-Optic Microsphere-Based Arrays for Multiplexed Biological Warfare Agent Detection. *Anal. Chem.* **2006**, *78*, 1023−1033.

(9) Nicewarner-Pena, S. R.; Freeman, R. G.; Reiss, B. D.; He, L.; Peña, D. J.; Walton, I. D.; Cromer, R.; Keating, C. D.; Natan, M. J. Submicrometer Metallic Barcodes. *Science* **2001**, *294*, 137−141.

(10) Liu, X.; Aizen, R.; Freeman, R.; Yehezkeli, O.; Willner, I. Multiplexed Aptasensors and Amplified DNA Sensors Using Functionalized Graphene Oxide: Application for Logic Gate Operations. *ACS Nano* **2012**, *6*, 3553−3563.

(11) Zhang, Y.; Zheng, B.; Zhu, C.; Zhang, X.; Tan, C.; Li, H.; Chen, B.; Yang, J.; Chen, J.; Huang, Y.; Wang, L.; Zhang, H. Single-Layer Transition Metal Dichalcogenide Nanosheet-Based Nanosensors for Rapid, Sensitive, and Multiplexed Detection of DNA. *Adv. Mater.* **2015**, *27*, 935−939.

(12) Gill, R.; Zayats, M.; Willner, I. Semiconductor Quantum Dots for Bioanalysis. *Angew. Chem., Int. Ed.* **2008**, *47*, 7602−7625.

(13) Freeman, R.; Liu, X.; Willner, I. Amplified Multiplexed Analysis of DNA by the Exonuclease III-Catalyzed Regeneration of the Target DNA in the Presence of Functionalized Semiconductor Quantum Dots. *Nano Lett.* **2011**, *11*, 4456−4461.

(14) Enkin, N.; Wang, F.; Sharon, E.; Albada, H. B.; Willner, I. Multiplexed Analysis of Genes Using Nucleic Acid-Stabilized Silver-Nanocluster Quantum Dots. *ACS Nano* **2014**, *8*, 11666−11673.

(15) Enkin, N.; Sharon, E.; Golub, E.; Willner, I. Ag Nanocluster/DNA Hybrids: Functional Modules for the Detection of Nitroaromatic and RDX Explosives. *Nano Lett.* **2014**, *14*, 4918−4922.

(16) Freeman, R.; Liu, X.; Willner, I. Chemiluminescent and Chemiluminescence Resonance Energy Transfer (CRET) Detection of DNA, Metal Ions, and Aptamer−Substrate Complexes Using Hemin/G-Quadruplexes and CdSe/ZnS Quantum Dots. *J. Am. Chem. Soc.* **2011**, *133*, 11597−11604.

(17) Liu, X.; Freeman, R.; Golub, E.; Willner, I. Chemiluminescence and Chemiluminescence Resonance Energy Transfer (CRET) Aptamer Sensors Using Catalytic Hemin/G-Quadruplexes. *ACS Nano* **2011**, *5*, 7648−7655.

(18) Hansen, J. A.; Wang, J.; Kawde, A.-N.; Xiang, Y.; Gothelf, K. V.; Collins, G. Quantum-Dot/Aptamer-Based Ultrasensitive Multi-Analyte Electrochemical Biosensor. *J. Am. Chem. Soc.* **2006**, *128*, 2228−2229.

(19) Hildebrandt, N. Biofunctional Quantum Dots: Controlled Conjugation for Multiplexed Biosensors. *ACS Nano* **2011**, *5*, 5286−5290.

(20) Wang, J.; Liu, G.; Merkoçi, A. Electrochemical Coding Technology for Simultaneous Detection of Multiple DNA Targets. *J. Am. Chem. Soc.* **2003**, *125*, 3214−3215.

(21) Du, Y.; Chen, C.; Zhou, M.; Dong, S.; Wang, E. Microfluidic Electrochemical Aptameric Assay Integrated On-Chip: A Potentially Convenient Sensing Platform for the Amplified and Multiplex Analysis of Small Molecules. *Anal. Chem.* **2011**, *83*, 1523−1529.

(22) Wang, F.; Elbaz, J.; Orbach, R.; Magen, N.; Willner, I. Amplified Analysis of DNA by the Autonomous Assembly of Polymers Consisting of DNAzyme Wires. *J. Am. Chem. Soc.* **2011**, *133*, 17149−17151.

(23) Tian, Y.; He, Y.; Mao, C. Cascade Signal Amplification for DNA Detection. *ChemBioChem* **2006**, *7*, 1862−1864.

(24) Wang, F.; Lu, C.-H.; Liu, X.; Freage, L.; Willner, I. Amplified and Multiplexed Detection of DNA Using the Dendritic Rolling Circle Amplified Synthesis of DNAzyme Reporter Units. *Anal. Chem.* **2014**, *86*, 1614−1621.

(25) Wang, F.; Freage, L.; Orbach, R.; Willner, I. Autonomous Replication of Nucleic Acids by Polymerization/Nicking Enzyme/DNAzyme Cascades for the Amplified Detection of DNA and the Aptamer−Cocaine Complex. *Anal. Chem.* **2013**, *85*, 8196−8203.

(26) Seeman, N. C.; Sleiman, H. F. DNA Nanotechnology. *Nat. Rev. Mater.* **2018**, *3*, 17068.

(27) Lu, C.-H.; Willner, B.; Willner, I. DNA Nanotechnology: From Sensing and DNA Machines to Drug-Delivery Systems. *ACS Nano* **2013**, *7*, 8320−8332.

(28) Chen, C.; Geng, J.; Pu, F.; Yang, X.; Ren, J.; Qu, X. Polyvalent Nucleic Acid/Mesoporous Silica Nanoparticle Conjugates: Dual Stimuli-Responsive Vehicles for Intracellular Drug Delivery. *Angew. Chem., Int. Ed.* **2011**, *50*, 882−886.

(29) Zhang, P.; Cheng, F.; Zhou, R.; Cao, J.; Li, J.; Burda, C.; Min, Q.; Zhu, J.-J. DNA-Hybrid-Gated Multifunctional Mesoporous Silica Nanocarriers for Dual-Targeted and MicroRNA-Responsive Controlled Drug Delivery. *Angew. Chem., Int. Ed.* **2014**, *53*, 2371−2375.

(30) Zhang, Z.; Balogh, D.; Wang, F.; Willner, I. Smart Mesoporous SiO_2 Nanoparticles for the DNAzyme-Induced Multiplexed Release of Substrates. *J. Am. Chem. Soc.* **2013**, *135*, 1934−1940.

(31) Lu, C.-H.; Willner, I. Stimuli-Responsive DNA-Functionalized Nano-/Microcontainers for Switchable and Controlled Release. *Angew. Chem., Int. Ed.* **2015**, *54*, 12212−12235.

(32) Chen, W.-H.; Liao, W.-C.; Sohn, Y. S.; Fadeev, M.; Cecconello, A.; Nechushtai, R.; Willner, I. Stimuli-Responsive Nucleic Acid-Based Polyacrylamide Hydrogel-Coated Metal-Organic Framework Nanoparticles for Controlled Drug Release. *Adv. Funct. Mater.* **2018**, *28*, 1705137.

(33) Chen, W.-H.; Luo, G.-F.; Vázquez-González, M.; Cazelles, R.; Sohn, Y. S.; Nechushtai, R.; Mandel, Y.; Willner, I. Glucose-

Responsive Metal−Organic-Framework Nanoparticles Act as "Smart" Sense-and-Treat Carriers. *ACS Nano* **2018**, *12*, 7538−7545.
(34) Chen, W.-H.; Yu, X.; Cecconello, A.; Sohn, Y. S.; Nechushtai, R.; Willner, I. Stimuli-Responsive Nucleic Acid-Functionalized Metal−Organic Framework Nanoparticles Using pH- and Metal-Ion-Dependent DNAzymes as Locks. *Chem. Sci.* **2017**, *8*, 5769−5780.
(35) Chen, W.-H.; Yu, X.; Liao, W.-C.; Sohn, Y. S.; Cecconello, A.; Kozell, A.; Nechushtai, R.; Willner, I. ATP-Responsive Aptamer-Based Metal-Organic Framework Nanoparticles (NMOFs) for the Controlled Release of Loads and Drugs. *Adv. Funct. Mater.* **2017**, *27*, 1702102.
(36) Liao, W.-C.; Riutin, M.; Parak, W. J.; Willner, I. Programmed pH-Responsive Microcapsules for the Controlled Release of CdSe/ZnS Quantum Dots. *ACS Nano* **2016**, *10*, 8683−8689.
(37) Liao, W.-C.; Sohn, Y. S.; Riutin, M.; Cecconello, A.; Parak, W. J.; Nechushtai, R.; Willner, I. The Application of Stimuli-Responsive VEGF- and ATP-Aptamer-Based Microcapsules for the Controlled Release of an Anticancer Drug, and the Selective Targeted Cytotoxicity toward Cancer Cells. *Adv. Funct. Mater.* **2016**, *26*, 4262−4273.
(38) Pinheiro, A. V.; Han, D.; Shih, W. M.; Yan, H. Challenges and Opportunities for Structural DNA Nanotechnology. *Nat. Nanotechnol.* **2011**, *6*, 763−772.
(39) Andersen, E. S.; Dong, M.; Nielsen, M. M.; Jahn, K.; Subramani, R.; Mamdouh, W.; Golas, M. M.; Sander, B.; Stark, H.; Oliveira, C. L. P.; Pedersen, J. S.; Birkedal, V.; Besenbacher, F.; Gothelf, K. V.; Kjems, J. Self-Assembly of a Nanoscale DNA Box with a Controllable Lid. *Nature* **2009**, *459*, 73−76.
(40) Wang, X.; Chandrasekaran, A. R.; Shen, Z.; Ohayon, Y. P.; Wang, T.; Kizer, M. E.; Sha, R.; Mao, C.; Yan, H.; Zhang, X.; Liao, S.; Ding, B.; Chakraborty, B.; Jonoska, N.; Niu, D.; Gu, H.; Chao, J.; Gao, X.; Li, Y.; Ciengshin, T.; Seeman, N. C. Paranemic Crossover DNA: There and Back Again. *Chem. Rev.* **2019**, *119*, 6273−6289.
(41) Mao, C.; Sun, W.; Seeman, N. C. Designed Two-Dimensional DNA Holliday Junction Arrays Visualized by Atomic Force Microscopy. *J. Am. Chem. Soc.* **1999**, *121*, 5437−5443.
(42) Goodman, R. P.; Schaap, I. A. T.; Tardin, C. F.; Erben, C. M.; Berry, R. M.; Schmidt, C. F.; Turberfield, A. J. Rapid Chiral Assembly of Rigid DNA Building Blocks for Molecular Nanofabrication. *Science* **2005**, *310*, 1661−1665.
(43) Goodman, R. P.; Berry, R. M.; Turberfield, A. J. The Single-Step Synthesis of a DNA Tetrahedron. *Chem. Commun.* **2004**, 1372.
(44) Goodman, R. P.; Heilemann, M.; Doose, S.; Erben, C. M.; Kapanidis, A. N.; Turberfield, A. J. Reconfigurable, Braced, Three-Dimensional DNA Nanostructures. *Nat. Nanotechnol.* **2008**, *3*, 93−96.
(45) Zhou, Z.; Zhang, P.; Yue, L.; Willner, I. Triggered Interconversion of Dynamic Networks Composed of DNA-Tetrahedra Nanostructures. *Nano Lett.* **2019**, *19*, 7540−7547.
(46) Pei, H.; Lu, N.; Wen, Y.; Song, S.; Liu, Y.; Yan, H.; Fan, C. A DNA Nanostructure-Based Biomolecular Probe Carrier Platform for Electrochemical Biosensing. *Adv. Mater.* **2010**, *22*, 4754−4758.
(47) Walsh, A. S.; Yin, H.; Erben, C. M.; Wood, M. J. A.; Turberfield, A. J. DNA Cage Delivery to Mammalian Cells. *ACS Nano* **2011**, *5*, 5427−5432.
(48) Li, J.; Pei, H.; Zhu, B.; Liang, L.; Wei, M.; He, Y.; Chen, N.; Li, D.; Huang, Q.; Fan, C. Self-Assembled Multivalent DNA Nanostructures for Noninvasive Intracellular Delivery of Immunostimulatory CpG Oligonucleotides. *ACS Nano* **2011**, *5*, 8783−8789.
(49) Peng, P.; Du, Y.; Zheng, J.; Wang, H.; Li, T. Reconfigurable Bioinspired Framework Nucleic Acid Nanoplatform Dynamically Manipulated in Living Cells for Subcellular Imaging. *Angew. Chem., Int. Ed.* **2019**, *58*, 1648−1653.
(50) Pei, H.; Liang, L.; Yao, G.; Li, J.; Huang, Q.; Fan, C. Reconfigurable Three-Dimensional DNA Nanostructures for the Construction of Intracellular Logic Sensors. *Angew. Chem., Int. Ed.* **2012**, *51*, 9020−9024.
(51) He, L.; Lu, D.; Liang, H.; Xie, S.; Zhang, X.; Liu, Q.; Yuan, Q.; Tan, W. mRNA-Initiated, Three-Dimensional DNA Amplifier Able to Function inside Living Cells. *J. Am. Chem. Soc.* **2018**, *140*, 258−263.
(52) Bartel, D.; MicroRNAs, P. Target Recognition and Regulatory Functions. *Cell* **2009**, *136*, 215−233.
(53) Ameres, S. L.; Horwich, M. D.; Hung, J. H.; Xu, J.; Ghildiyal, M.; Weng, Z.; Zamore, P. D. Target RNA-Directed Trimming and Tailing of Small Silencing RNAs. *Science* **2010**, *328*, 1534−1539.
(54) Frampton, A. E.; Gall, T. M. H.; Castellano, L.; Stebbing, J.; Jiao, L. R.; Krell, J. Towards a Clinical Use of miRNAs in Pancreatic Cancer Biopsies. *Expert Rev. Mol. Diagn.* **2013**, *13*, 31−34.
(55) Ma, R.; Jiang, T.; Kang, X. Circulating MicroRNAs in Cancer: Origin, Function and Application. *J. Exp. Clin. Cancer Res.* **2012**, *31*, 38.
(56) Dong, H.; Zhang, J.; Ju, H.; Lu, H.; Wang, S.; Jin, S.; Hao, K.; Du, H.; Zhang, X. Highly Sensitive Multiple MicroRNA Detection Based on Fluorescence Quenching of Graphene Oxide and Isothermal Strand-Displacement Polymerase Reaction. *Anal. Chem.* **2012**, *84*, 4587−4593.
(57) Gong, X.; Wei, J.; Liu, J.; Li, R.; Liu, X.; Wang, F. Programmable Intracellular DNA Biocomputing Circuits for Reliable Cell Recognitions. *Chem. Sci.* **2019**, *10*, 2989−2997.
(58) Su, J.; Wu, F.; Xia, H.; Wu, Y.; Liu, S. Accurate Cancer Cell Identification and MicroRNA Silencing Induced Therapy Using Tailored DNA Tetrahedron Nanostructures. *Chem. Sci.* **2020**, *11*, 80−86.
(59) Roberts, R. J. Restriction Enzymes and Their Isoschizomers. *Nucleic Acids Res.* **1990**, *18*, 2331−2365.
(60) Ma, M.; Benimetskaya, L.; Lebedeva, I.; Dignam, J.; Takle, G.; Stein, C. A. Intracellular mRNA Cleavage Induced through Activation of RNase P by Nuclease-Resistant External Guide Sequences. *Nat. Biotechnol.* **2000**, *18*, 58−61.
(61) Feng, X.; Duan, X.; Liu, L.; Feng, F.; Wang, S.; Li, Y.; Zhu, D. Fluorescence Logic-Signal-Based Multiplex Detection of Nucleases with the Assembly of a Cationic Conjugated Polymer and Branched DNA. *Angew. Chem., Int. Ed.* **2009**, *48*, 5316−5321.
(62) Hu, J.; Liu, M.-H.; Zhang, C.-Y. Construction of Tetrahedral DNA-Quantum Dot Nanostructure with the Integration of Multistep Förster Resonance Energy Transfer for Multiplex Enzymes Assay. *ACS Nano* **2019**, *13*, 7191−7201.
(63) Jayasena, S.; Aptamers, D. An Emerging Class of Molecules that Rival Antibodies in Diagnostics. *Clin. Chem.* **1999**, *45*, 1628−1650.
(64) Osborne, S. E.; Matsumura, I.; Ellington, A. D. Aptamers as Therapeutic and Diagnostic Reagents: Problems and Prospects. *Curr. Opin. Chem. Biol.* **1997**, *1*, 5−9.
(65) Ho, H.-A.; Leclerc, M. Optical Sensors Based on Hybrid Aptamer/Conjugated Polymer Complexes. *J. Am. Chem. Soc.* **2004**, *126*, 1384−1387.
(66) Canoura, J.; Wang, Z.; Yu, H.; Alkhamis, O.; Fu, F.; Xiao, Y. No Structure-Switching Required: A Generalizable Exonuclease-Mediated Aptamer-Based Assay for Small-Molecule Detection. *J. Am. Chem. Soc.* **2018**, *140*, 9961−9971.
(67) Wen, Y.; Pei, H.; Wan, Y.; Su, Y.; Huang, Q.; Song, S.; Fan, C. DNA Nanostructure-Decorated Surfaces for Enhanced Aptamer-Target Binding and Electrochemical Cocaine Sensors. *Anal. Chem.* **2011**, *83*, 7418−7423.
(68) Xiao, Y.; Lubin, A. A.; Heeger, A. J.; Plaxco, K. W. Label-Free Electronic Detection of Thrombin in Blood Serum by Using an Aptamer-Based Sensor. *Angew. Chem., Int. Ed.* **2005**, *44*, 5456−5459.
(69) Willner, I.; Zayats, M. Electronic Aptamer-Based Sensors. *Angew. Chem., Int. Ed.* **2007**, *46*, 6408−6418.
(70) Pavlov, V.; Xiao, Y.; Shlyahovsky, B.; Willner, I. Aptamer-Functionalized Au Nanoparticles for the Amplified Optical Detection of Thrombin. *J. Am. Chem. Soc.* **2004**, *126*, 11768−11769.
(71) Famulok, M.; Mayer, G. Aptamer Modules as Sensors and Detectors. *Acc. Chem. Res.* **2011**, *44*, 1349−1358.
(72) Zhang, J.; Wang, L.; Zhang, H.; Boey, F.; Song, S.; Fan, C. Aptamer-Based Multicolor Fluorescent Gold Nanoprobes for Multiplex Detection in Homogeneous Solution. *Small* **2010**, *6*, 201−204.

https://dx.doi.org/10.1021/acsnano.0c04031
ACS Nano 2020, 14, 9021−9031